

Deep Neural Network-Enhanced Frequency-Constrained Optimal Power Flow with Multi-Governor Dynamics

Fan Jiang, *Student Member, IEEE*, Xingpeng Li, *Senior Member, IEEE*, and Pascal Van Hentenryck, *Senior Member, IEEE*

Abstract—To ensure frequency security in power systems, both the rate of change of frequency (RoCoF) and the frequency nadir (FN) must be explicitly accounted for in real-time frequency-constrained optimal power flow (FCOPF). However, accurately modeling system frequency dynamics through analytical formulations is challenging due to their inherent nonlinearity and complexity. To address this issue, deep neural networks (DNNs) are utilized to capture the nonlinear mapping between system operating conditions and key frequency performance metrics. In this paper, a DNN-based frequency prediction model is developed and trained using the high-fidelity time-domain simulation data generated in PSCAD/EMTDC. The trained DNN is subsequently transformed into an equivalent mixed-integer linear programming (MILP) form and embedded into the FCOPF problem as additional constraints to explicitly enforce frequency security, leading to the proposed DNN-FCOPF formulation. For benchmarking, two alternative models are considered: a conventional optimal power flow without frequency constraints and a linearized FCOPF incorporating system-level RoCoF and FN constraints. The effectiveness of the proposed method is demonstrated by comparing the solutions of these three models through extensive PSCAD/EMTDC time-domain simulations under various loading scenarios.

Index Terms—Deep neural network, frequency nadir, grid synchronous inertia, optimal power flow, rate of change of frequency, real-time economic dispatch, system frequency response.

I. INTRODUCTION

With the aim of reducing carbon emission worldwide, inverter-based resources are widely integrated in power systems, which significantly reduce system inertia and cause issues on system frequency stability [1]-[2]. To avoid this issue and improve system frequency response (SFR), system-level approaches such as frequency-constrained optimal power flow (FCOPF) have been extensively investigated, where frequency-related constraints are explicitly integrated into economic dispatch and operational planning [3].

SFR can be categorized into multiple stages according to their time scales: inertial response (IR) occurring within the first few seconds after a disturbance, primary response (PR) acting over seconds to tens of seconds, secondary response over tens of seconds to minutes, and tertiary response over minutes to hours [4]. While secondary frequency regulation requires automatic generation control (AGC) to adjust genera-

tor output references [5], IR and PR depend on system inertia and governor controls, which can be optimized prior to disturbances through FCOPF. Accordingly, this paper focuses on two critical frequency-stability indicators: the worst rate of change of frequency (RoCoF) and the frequency nadir (FN) to prevent generator protection actions [6].

To capture SFR, which means to obtain RoCoF and FN during system transient response, a large set of differential and algebraic equations must be solved. However, as a real-time generation dispatch framework, FCOPF must meet strict requirements on computational efficiency. As a result, frequency-related constraints must be simplified and linearized before being embedded into FCOPF. For RoCoF, most existing studies assume that the maximum magnitude of RoCoF occurs immediately after the disturbance, and thus RoCoF can be approximately derived from the generator swing equations leading to a linear RoCoF constraint [7]-[9].

With respect to FN constraints, reference [10] evaluated SFR performance by linearizing the governor ramping curve; however, this approach fails to capture essential frequency dynamics. To address this, a simplified low-order frequency dynamic model [11] was proposed to calculate the frequency dynamics analytically, identifying that the FN is primarily influenced by PR. Building on this research, references [12]-[14] derived a linear equation of active power imbalance to ensure frequency stability. Although this approach is widely adopted, it assumes a uniform response time constant across all governors and considers only the largest time constant, which may lead to inaccuracies in FN estimation. To improve precision, references [15]-[16] derived the FN from original governor control loops by solving differential-algebraic equations (DAEs). However, this method is computationally prohibitive and unsuitable for integration into large-scale optimal power flow (OPF) framework. In summary, existing approaches for RoCoF and FN evaluation are either computationally prohibitive or insufficiently accurate.

Deep neural networks (DNN) provide a promising approach to address the aforementioned challenges. DNN models can be trained offline using large-scale datasets, thereby achieving high prediction accuracy [17]. Once trained, these models can be embedded into optimization frameworks, such as unit commitment (UC) and OPF, to replace complex DAE-based nonlinear constraints. In the context of OPF, some studies attempt to solve the problem directly using DNN-based end-to-end approaches [18]-[20], whereas others employ DNN to approximate specific OPF constraints in order to enhance computational efficiency [21]-[23]. Existing research indicates that end-to-end DNN-based OPF solutions may result in

Fan Jiang and Xingpeng Li are with the Department of Electrical and Computer Engineering, University of Houston, Houston, TX, 77204, USA. (e-mails: fjiang6@uh.edu; xli83@central.uh.edu); Pascal Van Hentenryck is with the H. Milton Stewart School of Industrial and Systems Engineering, Georgia Institute of Technology, Atlanta, GA, 30332, USA (email: pascal.vanhenryck@isye.gatech.edu).

infeasible operating points, while approaches that substitute only selected constraints with DNN models do not suffer from this limitation [18]. Therefore, incorporating DNN to express frequency-stability constraints in FCOPF is a viable strategy to simultaneously improve both computational speed and solution accuracy.

Existing studies on constructing frequency constraints with DNN remain limited. Some works have applied this concept to UC problems. Reference [22] proposes a DNN-based FN predictor for UC and ensures system frequency security through an encoding framework. However, such UC-oriented approaches are not directly applicable to FCOPF, since system inertia can be adjusted through generator commitment decisions in UC, which is not feasible in real-time operation. For OPF-related problems, a DNN-based inertia management framework for FCOPF is introduced in [23]. Nevertheless, only the FN evaluation is replaced by a DNN predictor, while the RoCoF constraint is still modeled using a simplified linear expression.

Motivated by addressing these limitations, this paper proposes a DNN-based frequency predictor (DNN-FP) that simultaneously estimates both RoCoF and FN for FCOPF. The main contributions of this paper are summarized as follows:

- A DNN-FP for predicting RoCoF and FN is developed and trained using high-fidelity electromagnetic transient (EMT) simulation data. By explicitly capturing multi-governor dynamics, the model can achieve higher accuracy without the computational burden of DAEs.
- The trained DNN-FP is first piecewise-linearized and formulated as a set of mixed-integer linear constraints, and then embedded into FCOPF, resulting in the proposed DNN-based FCOPF (DNN-FCOPF) model that can guarantee frequency security with dispatch solutions.
- The performance of the proposed DNN-FCOPF and two benchmark models are evaluated against EMT simulation results, and comparisons of RoCoF and FN demonstrate that DNN-FCOPF significantly improve both computational efficiency and solution accuracy.

The remaining part of this paper is organized as follows. Section II demonstrates the DNN-FP and its data acquisition approach for frequency dynamics capture. In Section III, the proposed DNN-FCOPF and the two benchmark models, T-OPF without frequency constraints and L-FCOPF with linear RoCoF and FN constraints. The case studies for IEEE 9-bus and 39-bus systems are compared in Section IV. Section V presents the conclusions.

II. DEEP NEURAL NETWORK-BASED FREQUENCY PREDICTOR

This section introduces a DNN-based framework for predicting key frequency response indices, including RoCoF and FN, and details the approach used to construct the training data for model development.

A. DNN-Based Frequency Predictor

DNN is a class of artificial intelligence models characterized by multiple hidden layers between inputs and outputs. DNNs can adopt a variety of architectural configurations, among which the fully connected neural network is the simplest form, where each neuron in a given layer is connected to

all neurons in the adjacent layers. The structure is illustrated in Fig. 1, which is used as the frequency predictor in this paper.

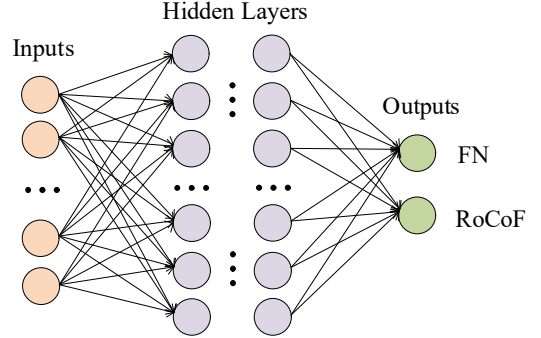


Fig. 1. Structure of the DNN-based frequency predictor.

For each layer of the DNN for frequency prediction, the neuron outputs are obtained by applying a polynomial mapping to the inputs from the previous layer, followed by a non-linear activation function, and the resulting outputs are then passed to the next layer. In this paper, the input features of this predictor include the active power outputs of all generators and the active power demands of all loads. The model outputs predict RoCoF and FN. The mathematical formulation of the DNN-FP predictor is given in (1)-(4). Rectified linear unit (ReLU) functions are adopted as the activation functions for all layers except the output layer that contains no activation functions, as defined in (3).

$$z_1 = xW_1 + b_1 \quad (1)$$

$$z_m = a_{m-1}W_m + b_m, 2 \leq m \leq N_L \quad (2)$$

$$a_m = \max(z_m, 0), 1 \leq m \leq N_L \quad (3)$$

$$r_h = a_{N_L}W_{N_L+1} + b_{N_L+1} \quad (4)$$

where, W_m and b_m denote the weight matrix and bias vector of the m -th layer, respectively; N_L represents the number of hidden layers; a_m is the activation output vector of the neurons of layer m ; z_m is the preactivated vector of a_m ; x denotes the input vector; and r_h is the output vector.

B. Training Data Acquisition Approach

Acquiring a high-quality dataset is critical for training the DNN-FP and improving its accuracy, as the quality of the dataset has a direct impact on the model's performance. In many existing studies, frequency response data following generator tripping are obtained by phasor-domain simulation platforms [21]-[22], which primarily models electromechanical dynamics rather than EMT phenomena. However, accurate evaluation of frequency response metrics requires EMT-level simulations to capture the complex, non-linear governor dynamics. PSCAD/EMTDC is a well-established commercial platform that is widely used for frequency transient studies in power systems. Accordingly, a PSCAD/EMTDC model is employed in this paper to generate the high-fidelity training dataset, ensuring that EMT dynamics are properly captured.

The training data are generated through a large number of independent simulation runs, considering variations in load levels, initial generator outputs, and the locations of the tripped generator. For each simulation, the RoCoF and FN are calculated. The RoCoF measurement window is typically selected between 5 and 10 cycles [24]; in this work, a 10-cycle window (0.167 s for a 60 Hz system) is adopted, and the worst

measured value within this window is used as the RoCoF label. It is worth noting that frequency response may vary at different buses; hence, the center of inertia (COI) [25] is applied to obtain system frequency and calculate RoCoF and FN. The equation of COI frequency can be expressed as

$$f_{COI} = \frac{\sum_{i \in \mathcal{G}} f_i H_i}{\sum_{i \in \mathcal{G}} H_i} \quad (5)$$

where \mathcal{G} denotes the set of generators, f_i represents the frequency measured at the bus of the i -th generator, and H_i denotes the inertia constant of i -th generator.

After collecting the RoCoF and FN for all simulated scenarios, the resulting dataset is used to train the DNN-FP. The trained model is subsequently reformulated and embedded into the FCOPF framework as frequency-related constraints. Details are presented in Section III. C.

III. OPTIMAL POWER FLOW FRAMEWORKS

This section describes the objective functions and constraints of three optimization formulations: (i) a traditional OPF (T-OPF) without any frequency-related constraints, (ii) a linearized system-wide FCOPF (L-FCOPF), and (iii) the proposed DNN-FCOPF incorporating a DNN-FP.

A. Traditional Optimal Power Flow

The objective of the OPF framework is to minimize the total operating cost, as expressed in (6), where a quadratic function is employed to represent the generator cost.

$$\min \sum_{i \in \mathcal{G}} (c_{2,i} P_i^2 + c_{1,i} P_i + c_{0,i}) \quad (6)$$

where $c_{2,i}$, $c_{1,i}$, $c_{0,i}$ are generator cost coefficients, and P_i is the active power output of i -th generator.

The constraints of the T-OPF consist of nodal power balance, power flow relations, generator output limits, and thermal limits of transmission lines, which are given in (7)-(10), respectively.

$$\sum P_{k,b}^{\text{fbus}} + P_b^{\text{load}} = \sum P_{k,b}^{\text{tbus}} + \sum P_{i,b}, \quad \forall b \in \mathcal{B} \quad (7)$$

$$P_k = \frac{\theta_p - \theta_q}{x_k}, \quad p, q \in \mathcal{B}, \quad \forall k \in \mathcal{K} \quad (8)$$

$$P_i^{\min} \leq P_i \leq P_i^{\max}, \quad \forall i \in \mathcal{G} \quad (9)$$

$$-P_k^{\text{thm}} \leq P_k \leq P_k^{\text{thm}}, \quad \forall k \in \mathcal{K} \quad (10)$$

where \mathcal{B} and \mathcal{K} denote the sets of buses and transmission lines respectively; $P_{k,b}^{\text{fbus}}$ and $P_{k,b}^{\text{tbus}}$ represent the active power flowing from and to bus b ; P_k denotes the active power flow on line k ; P_i^{\min} and P_i^{\max} are minimum and maximum active power limits of generator i ; P_b^{load} is the active power demand at bus b ; P_k^{thm} is the thermal limit of transmission line k .

B. Linearized Frequency-Constrained Optimal Power Flow

Most Independent System Operators (ISOs) solve the optimal power flow (OPF) problem in real time at regular intervals, typically every 5 minutes, which places stringent requirements on computational efficiency. In addition, SFR are governed by high-order inertial components, making direct exact evaluation with detailed frequency response equations computationally expensive. As a result, SFR models in FCOPF are commonly simplified through linearization.

1) *RoCoF calculation*: It is generally recognized that the worst RoCoF occurs at the instant of a generator outage [7]-[9]. Based on this premise, the RoCoF can be approximated using the generator swing equation, as given in (11).

$$\Delta P_m - \Delta P_e = \frac{2P_{\text{base}} \sum_{i \in \mathcal{G}} H_i}{f_0} \frac{df}{dt} \quad (11)$$

where, ΔP_m and ΔP_e denote the changes in mechanical input power and electrical output power, respectively; P_{base} is the system active power base; and f_0 denotes the nominal system frequency.

For a short interval immediately following the disturbance, the mechanical input power ΔP_m is assumed to remain constant, while the electrical output power ΔP_e changes instantaneously. Consequently, the worst RoCoF can be expressed as:

$$\frac{df}{dt} = -\frac{f_0}{2P_{\text{base}} \sum_{i \in \mathcal{G}} H_i} P_d \quad (12)$$

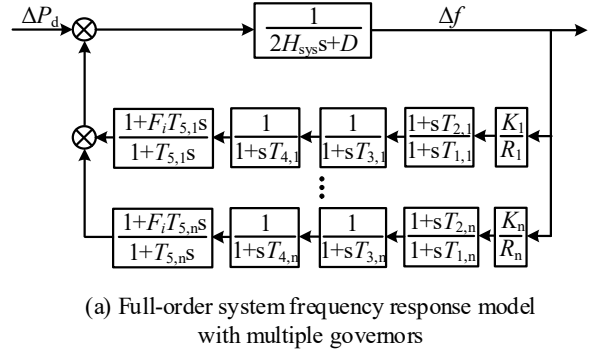
where P_d denotes the pre-disturbance output power of the tripped generator.

Accordingly, the RoCoF constraint can be written as:

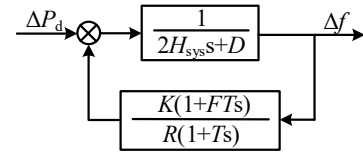
$$-\frac{f_0}{2P_{\text{base}} \sum_{i \in \mathcal{G}} H_i} P_d \geq R_{\text{lmt}} \quad (13)$$

where R_{lmt} denotes the RoCoF security limit.

2) *FN calculation*: The typical full-order SFR model for a large-scale power system dominated by reheat turbine governors is illustrated in Fig. 2 (a), which contains multiple integral elements [5]. To facilitate simplified estimation of frequency behavior, P.M. Anderson *et al.* proposed a low-order SFR model, as shown in Fig. 2 (b), in which nonlinearities and all time constants except the dominant ones in the generating unit equations are neglected [11]. For a multi-machine system, the time constants T of all governors are assumed as the same [5], [13]. $T_{1,i} - T_{5,i}$ denote time constants and $i = 1, 2, \dots, n$, F_i is the fraction of total power generated by the high-pressure turbine of i -th generator and F stands for the power fraction in the aggregated low-order model. K_i is mechanical power gain factor, and R_i represents the droop control gain of the i -th generator. R , T , and K are relative aggregated parameters for the low-order model. D denotes the system damping constant, and H_{sys} stands for the system inertia.



(a) Full-order system frequency response model with multiple governors



(b) Low-order system frequency response model

Fig. 2. System frequency response models of (a) full-order, and (b) low-order.

Under a step power imbalance disturbance, i.e., $\Delta P_e(s) = -\Delta P_d/s$, the frequency response in the time domain can be expressed as (14).

$$\Delta f(t) = -\frac{\Delta P_e}{2H_{sys}T\omega_n^2} - \frac{\Delta P_e}{2H_{sys}\omega_d} e^{-\xi\omega_n t} [\sin(\omega_d t) - \frac{1}{\omega_d T} \sin(\omega_d t + \varphi)] \quad (14)$$

in which,

$$H_{sys} = \frac{\sum_{i \in \mathcal{G}} H_i P_i^{\max}}{\sum_{i \in \mathcal{G}} P_i^{\max}} \quad (15)$$

$$\omega_n = \sqrt{\frac{D+R}{2H_{sys}T}} \quad (16)$$

$$\omega_d = \omega_n \sqrt{1 - \xi^2} \quad (17)$$

$$\xi = \frac{2H_{sys} + T(D+R)}{2\sqrt{2H_{sys}T(D+R)}} \quad (18)$$

$$\varphi = \sin^{-1}(\sqrt{1 - \xi^2}) \quad (19)$$

$$F = \sum_{i \in \mathcal{G}} \frac{K_i F_i P_i^{\max}}{R_i \sum_{i \in \mathcal{G}} P_i^{\max}} \quad (20)$$

$$R = \sum_{i \in \mathcal{G}} \frac{K_i P_i^{\max}}{R_i \sum_{g \in \mathcal{G}} P_g^{\max}} \quad (21)$$

$$T = \frac{\sum_{i \in \mathcal{G}} T_{5,i} P_i^{\max}}{\sum_{i \in \mathcal{G}} P_i^{\max}} \quad (22)$$

where ω_n stands for the natural frequency, ω_d represents the damped natural frequency, ξ denotes the damping ratio, and φ is the phase angle associated with the damped oscillatory component of SFR.

It is noteworthy that as only the primary time constants among T_1 through T_5 in the full-order model are considered as the time constant in the low-order SFR model, the effective time constant T is defined as the capacity-weighted average of T_5 across all participating generators.

To obtain the FN during frequency response, the derivative of (14) is taken, as shown in (23).

$$\frac{d\Delta f(t)}{dt} = 0 \quad (23)$$

Assuming the disturbance occurs at time $t = 0$, the instant at which the frequency reaches its worst value FN can be expressed as (24).

$$t_{nadir} = \frac{1}{\omega_d} \tan^{-1} \left(\frac{\omega_d T}{\xi \omega_d T - 1} \right) \quad (24)$$

Then the frequency deviation can be written as (25).

$$\Delta f = -\frac{\Delta P_e}{R+D} \left(1 + e^{-\xi \omega_n t_{nadir}} \sqrt{\frac{T(R-F)}{2H_{sys}}} \right) \quad (25)$$

(25) is linear with respect to ΔP_e , and can therefore be incorporated into FCOPF formulation through constraint (26).

$$f_0 - \frac{\Delta P_e}{R+D} \left(1 + e^{-\xi \omega_n t_{nadir}} \sqrt{\frac{T(R-F)}{2H_{sys}}} \right) \geq f_{lmt} \quad (26)$$

In summary, the L-FCOPF is an enhanced T-OPF with extra frequency constraints given in (13) and (26). The L-FCOPF and T-OPF are implemented as baseline models for comparisons with the proposed DNN-FCOPF model.

C. Proposed DNN-FCOPF Model with DNN-FP

The L-FCOPF may not provide sufficient accuracy due to the following assumptions: 1) the worst RoCoF occurs immediately after the disturbance; 2) only the dominant time constant of the governor control is considered; and 3) all governors are assumed to share the same time constant. To achieve higher accuracy in representing SFR, the DNN-based frequency predictor (DNN-FP) is incorporated into the FCOPF framework.

In DNN-FP, the activation function (3) is nonlinear. Generally, it can be exactly linearized using the BigM method [28], as shown in (27)-(30).

$$a_m \leq z_m - h_l(1 - B_m) \quad (27)$$

$$a_m \geq z_m \quad (28)$$

$$a_m \leq h_u B_m \quad (29)$$

$$a_m \geq 0 \quad (30)$$

where h_u and h_l are the lower boundary and upper boundary of the value of all possible z_m , and B_m is a binary variable.

By applying this BigM linearization approach, the DNN-FP can be embedded into the FCOPF formulation without loss of accuracy, thereby transforming the resulting DNN-FCOPF into a mixed-integer linear programming (MILP) problem.

The outputs of the DNN-FP, namely frequency nadir FN^{DNN} and $RoCoF^{DNN}$, as illustrated in Fig. 1, must also be constrained when incorporated into DNN-FCOPF as shown in (31)-(32).

$$RoCoF^{DNN} \geq R_{lmt} \quad (31)$$

$$FN^{DNN} \leq f_{lmt} \quad (32)$$

Therefore, the DNN-FCOPF is enhancing T-OPF with additional constraints (1)-(2), (4), (27)-(32).

To summarize, the objective and constraints of the three OPF models are presented in TABLE I.

TABLE I
OBJECTIVES AND CONSTRAINTS OF T-OPF, L-FCOPF AND DNN-FCOPF

| Model | Objective | Shared Constraints | Unique Constraints |
|-----------|-----------|--------------------|-------------------------|
| T-OPF | | | None |
| L-FCOPF | (6) | (7)-(10) | (13), (26) |
| DNN-FCOPF | | | (1)-(2), (4), (27)-(32) |

IV. CASE STUDIES

This section aims to verify the effectiveness and accuracy of the proposed DNN-FCOPF framework through the comparisons with two benchmark OPF models, namely T-OPF and L-FCOPF, on the IEEE 9-bus and 39-bus standard test systems.

A. IEEE 9-Bus System

The topology of the modified IEEE 9-bus system is illustrated in Fig. 3, and the system parameters are provided in [29]. The sum of generator outputs at bus 1, 2 and 3 are 72MW, 163MW and 85MW respectively. Generators on bus 1, 2 and 3 are split into multiple different generators: two at bus 1, four at bus 2, and three at bus 3. This aims to maintain the contingency capacity between 10% and 15%, preventing the severe disturbances which is infrequent and impractical in real power systems. It is notable that the generators at the same bus are identical in all aspects, including rated capacity, governor response control, and cost function, so they have the same outputs. Each generator output can be calculated by dividing the number of generators at its terminal bus. The real power of the original loads at bus 5, 6 and 8 are: 125MW, 90MW, and 100MW respectively.

The parameters of the full-order SFR model in Fig. 2(b) of each generator are shown in Table II, where $m = 1, 2, j = 1, 2, 3, 4$, and $p = 1, 2, 3$ denoting the corresponding indices.

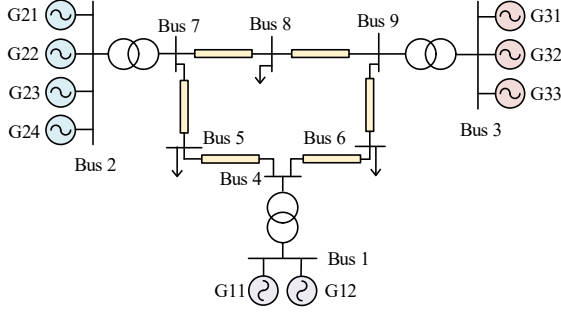


Fig. 3. Illustration of a modified IEEE 9-bus system.

TABLE II.
PARAMETERS IN THE FULL-ORDER FREQUENCY RESPONSE MODEL

| Gen | T_1 | T_2 | T_3 | T_4 | T_5 | F | K | R |
|------|-------|-------|-------|-------|-------|-------|-----|------|
| G1m | 0.15 | 0.05 | 0.3 | 0.26 | 8 | 0.27 | 1 | 0.05 |
| G2ji | 0.1 | 0 | 0.259 | 0.1 | 10 | 0.272 | 1 | 0.05 |
| G3pi | 0.083 | 0 | 0.2 | 0.05 | 5 | 0.28 | 1 | 0.05 |

Based on the modified IEEE 9-bus system, T-OPF, L-FCOPF and DNN-FCOPF are implemented according to the objective and constraints in Table I. All the settings are the same for these three models, except the frequency related constraints. The following provides a detailed procedure for establishing and validating the proposed DNN-FCOPF model.

1) Training of DNN-FP:

The accuracy of the frequency performance estimates produced by the DNN-FP has a significant impact on the dispatch results of the DNN-FCOPF, making it essential to train a well-performing model.

The development of DNN-FP requires a training dataset obtained from a reliable source. To this end, a high-fidelity real-time simulation model of the modified IEEE 9 bus system is established in PSCAD/EMTDC. WSCC Type G governor [30] is used as the governor control, while the exciter model is IEEE AC5C [31]. It is noteworthy that although the governor control structures are identical across all generators, indicating a system dominated by reheated steam turbines, their specific parameter sets, such as time constants, differ across units. This diversity in control parameters ensures a more realistic representation of the varying response characteristics of individual generating units during frequency disturbances.

To meet the $N-1$ requirement, the sudden outage of an arbitrary generator is modeled as the credible contingency. For different data points, the loads in this model vary from 80% to 120% of original base-case load values. Then, the dataset is acquired through this time-domain EMT model. Each data point consists of the RoCoF and FN for a given scenario, along with its corresponding conditions, including loads, generator outputs, and contingency locations. This EMT model can also serve as a reference for validating the frequency performance of the dispatch solutions obtained with the above-mentioned three OPF models.

Using the dataset generated from the high-fidelity simulation model, the training process adopts the mean square error (MSE) as the loss function, which is defined in (33).

$$\mathcal{L} = \frac{1}{n} \sum (r_h - r_{true})^2 \quad (33)$$

where n is the number of data points, r_{true} stands for true output value of each data point.

2) Validation of DNN-FP:

The performance of the proposed DNN model is evaluated using both the training loss evolution and the comparison between test targets and model predictions, which are shown in Fig. 4. As illustrated in the training and validation loss curves in Fig. 4 (a), the loss decreases steadily and converges to a stable value without noticeable oscillations, indicating effective learning and good convergence behavior. Furthermore, the comparisons between the predicted outputs and the ground-truth test data of RoCoF and FN in Fig. 4 (b) and (c) show a high degree of consistency across all samples, with no evident systematic bias or large deviations. These results demonstrate that the proposed DNN-FP is capable of accurately capturing the complex frequency dynamics and exhibits strong generalization performance on unseen data.

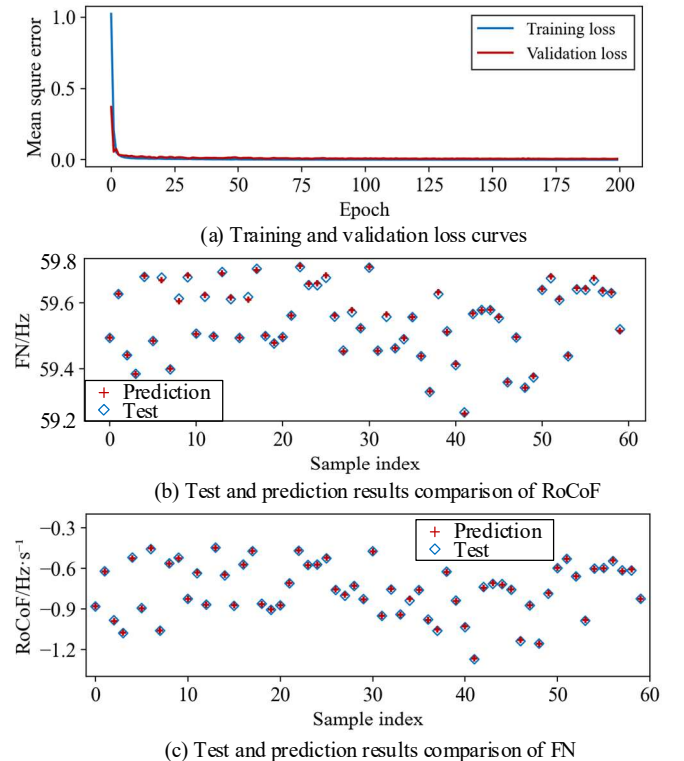


Fig. 4. (a) Training and validation loss curves, and test and prediction results comparison of (b) RoCoF, and (c) FN, of the DNN-FP.

Therefore, the proposed DNN-FP offers a high level of accuracy in forecasting both RoCoF and FN, and is suitable to be incorporated into OPF models.

3) Development of DNN-FCOPF:

After validating the effectiveness of the DNN-FP, the model is reformulated and embedded into the DNN-FCOPF framework. The proposed optimization model, along with the two benchmark models, T-OPF and L-FCOPF, is implemented in Python 3.9 using Gurobi as the solver. All optimization models share identical parameter settings; and the RoCoF limit R_{lmt} and FN limit f_{lmt} in both the L-FCOPF and DNN-FCOPF models are set to -0.5Hz/s and 59.5Hz, respectively [8]. All optimization problems are solved on a computer equipped with a 12th Gen Intel® Core™ i7-12700 CPU @ 2.1 GHz and 32.0 GB of RAM.

4) Validation of DNN-FCOPF:

The effectiveness and universality of the DNN-FCOPF are verified through comparisons with both high-fidelity EMT simulation results and the outcomes of the two benchmark OPF models.

To evaluate the performance across a full operational cycle, a 24-hour load profile is applied to the three optimization models. This profile is derived from actual system demand data provided by the Electric Reliability Council of Texas (ERCOT) [32]. The load profile is shown in Fig. 5.

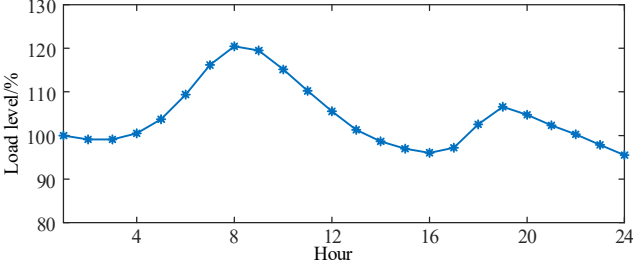


Fig. 5. 24-hour load profile from ERCOT.

Following the formulation of the optimization models, a worst-case contingency scenario is defined: the sudden outage of generator G11 at $t = 0$ s. This specific event is selected as it represents the most critical contingency, characterized by the largest loss of generation and the most severe impact on system frequency stability.

The three optimization models, namely T-OPF, L-FCOPF and the proposed DNN-FCOPF, are solved under the aforementioned scenarios. The resulting dispatch solutions determine the generator output setpoints. These setpoints are then applied as generator reference values in the PSCAD/EMTDC simulation model, and the corresponding frequency responses including RoCoF and FN, are recorded. The 24-hour RoCoF and FN trajectories, simulated using generator power references from the three optimization models, are compared in Fig. 6. The discrepancies between simulated and predicted dispatch results for the L-FCOPF and DNN-FCOPF models are illustrated in Fig. 7; the T-OPF model is excluded from this analysis due to its lack of frequency prediction outputs.

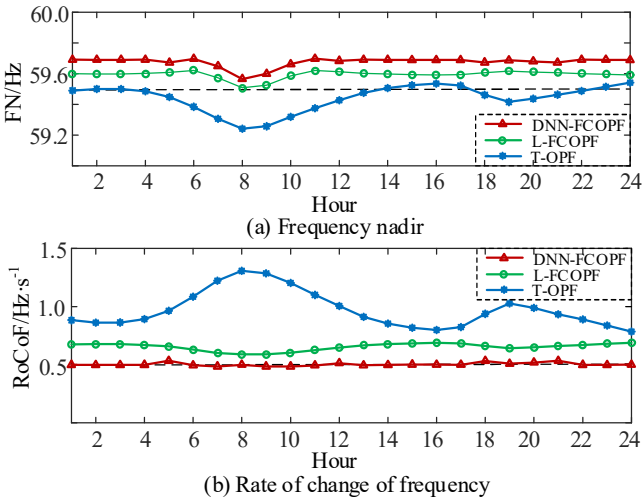


Fig. 6. Comparisons over 24 hourly scenarios in terms of metrics (a) FN, (b) RoCoF profiles, obtained from EMT simulations for the IEEE 9-bus system, under T-OPF, L-FCOPF, and DNN-FCOPF frameworks.

As shown in Fig. 6, the RoCoF and FN simulation results for the proposed DNN-FCOPF framework strictly adhere to operational limits, whereas the T-OPF and L-FCOPF models exhibit limit violations. In the T-OPF case, significant limit violations occur, indicating that frequency stability requirements are unmet, which could lead to severe cascading outages. Although L-FCOPF outperforms T-OPF, its results still exceed the permissible thresholds. The analysis of the predicted SFR results reveals that for L-FCOPF, only the FN constraints are active while the RoCoF constraints remain inactive. Conversely, in the DNN-FCOPF model, the RoCoF constraints are binding, whereas the FN constraints are non-binding. Consequently, the SFR in the DNN-FCOPF framework is primarily governed by RoCoF limitations, with the FN remaining well within safety margins. This demonstrates that the proposed DNN-FCOPF provides a more effective mechanism for constraining the SFR, thereby significantly enhancing overall system frequency stability.

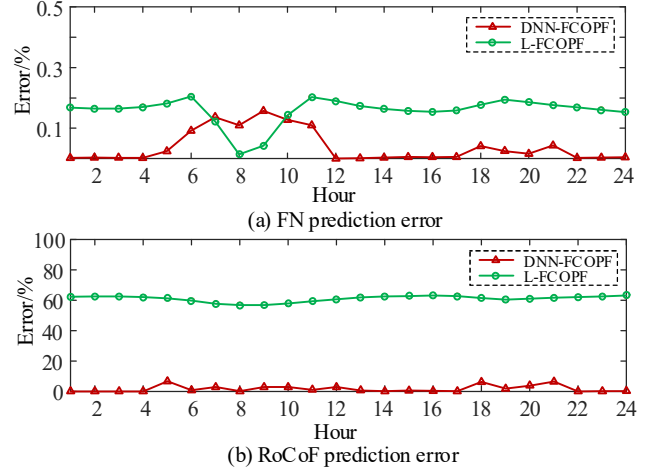


Fig. 7. Relative errors of (a) FN, (b) RoCoF between EMT simulation results and predicted dispatch results under L-FCOPF and DNN-FCOPF.

In Fig. 7, the definitions of the RoCoF and FN errors are given in (34). The results obtained from high-fidelity EMT simulations are used as reference values, as they most accurately represent the SFR under real-world operating conditions.

$$E_r = \left| \frac{y_d - y_s}{y_s} \right| \times 100\% \quad (34)$$

where y_d is the dispatch result from optimization model and y_s represents the result from the EMT simulation.

As illustrated in Fig. 7, the prediction accuracy for RoCoF in the proposed DNN-FCOPF significantly surpasses that of the L-FCOPF model. Specifically, RoCoF errors in the L-FCOPF approach reach approximately 60%, whereas the DNN-FCOPF consistently exhibits errors below 5%. While both models exhibit FN errors under 1%, the DNN-FCOPF generally outperforms linearized FN constraints. Notably, although the L-FCOPF occasionally shows smaller FN errors than the DNN-FCOPF in specific cases, these fluctuations in the proposed DNN-FCOPF model do not compromise system frequency security because the RoCoF constraints are binding for the DNN-FCOPF and, the FN remains well within safety margins. Conversely, in the L-FCOPF framework, the inaccuracy of RoCoF prediction leads to the RoCoF constraints being deemed inactive, meaning FN errors can directly undermine

frequency stability. These results suggest that while linearized FN approximations are relatively accurate, linearized RoCoF constraints lack the necessary precision for reliable stability assessment. In contrast, the proposed DNN-FP achieves high accuracy for both critical parameters. These comparisons validate both the effectiveness and the generalizability of the proposed framework across diverse operating conditions.

To provide a more granular assessment of the frequency stability improvement performance across the three optimization models, a valley Hour 1 and a peak Hour 8 are selected for detailed comparative analysis.

Under the 100% load condition in Hour 1, the dispatch outcomes and resulting frequency responses for the T-OPF, L-FCOPF, and DNN-FCOPF models are summarized in Table III.

As summarized in Table IV, the DNN-FCOPF framework yields significantly smaller prediction errors for both RoCoF and FN compared to the L-FCOPF model. In the absence of frequency stability constraints, the T-OPF model results in the lowest total operating cost, albeit at the expense of severe SFR degradation with increased grid instability risk. Conversely, the integration of frequency stability constraints in the L-FCOPF and DNN-FCOPF models leads to higher total costs and increased solve time; however, it ensures superior SFR performance. To further validate these findings, the detailed SFR trajectories obtained from high-fidelity EMT simulations in PSCAD/EMTDC are compared for all three optimization models in Fig. 8.

TABLE III.
RESULTS OF T-OPF, L-FCOPF AND DNN-FCOPF AT HOUR 1

| | Model | T-OPF | L-FCOPF | DNN-FCOPF |
|-------------------|---------------------------|---------|--------------------|------------------|
| OPF | Total Cost (\$) | 3,536.8 | 3,537.5 | 3,539.2 |
| | Solve Time (s) | 0.39 | 0.46 | 0.74 |
| | RoCoF (Hz/s) (% error) | N/A | -0.254 (62.31%) | -0.500 (0.2%) |
| | FN (Hz) (% error) | N/A | 59.50 (0.17%) | 59.69 (<0.1%) |
| EMT Simulation | RoCoF (Hz/s) | -0.883 | -0.674 | -0.499 |
| | FN (Hz) | 59.49 | 59.60 | 59.69 |

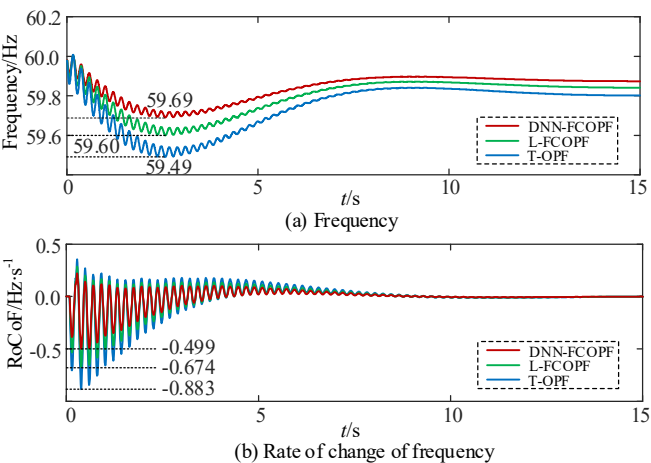


Fig. 8. (a) Frequency response curves and (b) RoCoF curves at Hour 1, using PSCAD/EMTDC, with initial grid conditions from T-OPF, L-FCOPF and DNN-FCOPF models respectively.

Fig. 8 compares the SFR trajectories for the three optimization models. The FN exhibits an improving trend, with values of 59.49 Hz, 59.60 Hz, and 59.69 Hz for the T-OPF, L-FCOPF, and DNN-FCOPF models, respectively. A similar improvement is observed in the RoCoF magnitudes, which are recorded at -0.883 Hz/s, -0.674 Hz/s, and -0.499 Hz/s, respectively. These results indicate that the frequency constraints within these three optimization frameworks exhibit progressively increasing stringency. Specifically, while the L-FCOPF model satisfies the FN requirement, it fails to maintain the RoCoF within permissible limits. In contrast, the proposed DNN-FCOPF successfully fulfills both stability requirements, ensuring a more robust frequency response.

TABLE IV.
RESULTS OF T-OPF, L-FCOPF AND DNN-FCOPF AT HOUR 8

| | Model | T-OPF | L-FCOPF | DNN-FCOPF |
|-------------------|---------------------------|---------|--------------------|-------------------|
| OPF | Total Cost (\$) | 4,056.7 | 4,065.2 | 4,068.2 |
| | Solve Time (s) | 0.38 | 0.41 | 0.72 |
| | RoCoF (Hz/s) (% error) | N/A | -0.254 (56.95%) | -0.500 (0.20%) |
| | FN (Hz) (% error) | N/A | 59.50 (<0.1%) | 59.50 (0.12%) |
| EMT Simulation | RoCoF (Hz/s) | -1.307 | -0.590 | -0.501 |
| | FN (Hz) | 59.24 | 59.51 | 59.57 |

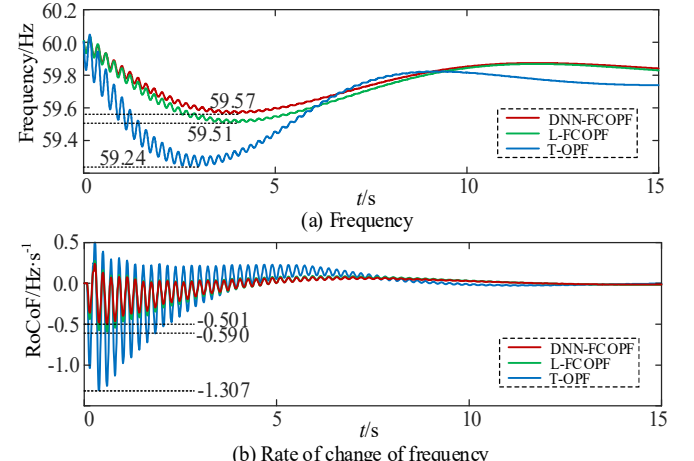


Fig. 9. (a) Frequency response curves and (b) RoCoF curves at Hour 8, using PSCAD/EMTDC, with initial grid conditions from T-OPF, L-FCOPF and DNN-FCOPF models respectively.

For Hour 8, which represents the peak load condition with a demand increase to approximately 120% of the nominal level, which is also the peak load, the resulting dispatch outcomes and EMT-simulated SFR metrics are summarized in Table IV. The corresponding time-domain SFR trajectories are compared in Fig. 9.

In this scenario, the trends for total operating cost and solve time remain consistent with the observations from Hour 1. Notably, all three optimization models result in some degree of RoCoF violation; however, the proposed DNN-FCOPF exhibits the minimum deviation. Although the RoCoF prediction error in the L-FCOPF is substantially higher than that of the DNN-FCOPF, the EMT simulation indicates that its RoCoF violation is relatively moderated compared to the un-

constrained T-OPF. This suggests that while linearized frequency constraints provide a certain degree of regulation, they lack the precision necessary for full compliance. Furthermore, while the L-FCOPF achieves higher prediction accuracy for FN, the slightly higher FN error in the DNN-FCOPF does not compromise security, as the simulated FN remains strictly within permissible limits. Ultimately, the DNN-FCOPF framework demonstrates superior overall accuracy and ensures the compliance of SFR.

In summary, case studies conducted on the IEEE 9-bus system demonstrate that the proposed DNN-FCOPF framework delivers superior SFR performance compared to both T-OPF and L-FCOPF. By maintaining critical frequency metrics within safety thresholds, the proposed approach significantly enhances overall system frequency stability.

B. IEEE 39-Bus System

To validate the robustness and scalability of the proposed DNN-FCOPF framework, case studies are conducted on the IEEE 39-bus system with 10 synchronous generators. The topology and parameters can be found in [33]. The governor control parameters in Table III are also used in this test system. The same 24-hour load profile is applied for the three optimization models. The contingency is assumed as the outage of the generator at bus 38 which has the maximum capacity. The FN and RoCoF EMT simulation outcomes of T-OPF, L-FCOPF and proposed DNN-FCOPF are compared in Fig. 10. The prediction errors of L-FCOPF and DNN-FCOPF are compared in

Fig. 10 and Fig. 11 present trends similar to those observed in the IEEE 9-bus case studies: DNN-FCOPF achieves the best performance, followed by L-FCOPF, demonstrating that the proposed DNN-FCOPF effectively enhances frequency stability. Specifically, Fig. 10 (a) shows that the FN values obtained from all three optimization models remain within the prescribed limits, indicating that the contingency is less severe than that of the IEEE 9-bus system. In contrast, Fig. 10 (b), reveals that the RoCoF values from time-domain simulations violate the limit in most intervals.

Fig. 11 illustrate the prediction errors for FN and RoCoF from the L-FCOPF and DNN-FCOPF models. As shown in Fig. 11 (a), while the FN error of L-FCOPF is marginally smaller in isolated instances, the proposed DNN-FCOPF maintains a consistently lower error across the majority of the operational horizon. Furthermore, Fig. 11 (b) demonstrates that the RoCoF prediction error for the DNN-FCOPF is uniformly lower than that of the L-FCOPF throughout all time intervals.

Among the three models, DNN-FCOPF exhibits the smallest prediction errors and violations, outperforming both T-OPF and L-FCOPF. These results underscore the necessity of incorporating detailed governor response dynamics into the FCOPF framework to ensure reliable frequency security and mitigate the risks associated with simplified modeling approximations.

The case studies conducted on IEEE 9-bus system and IEEE 39-bus system demonstrate that by capturing complex governor dynamics overlooked by linearized models, the DNN-FP enables the optimization framework to significantly enhance system frequency stability. Consequently, the DNN-FCOPF

achieves superior SFR performance and more reliable security margins compared to the conventional T-OPF and L-FCOPF.

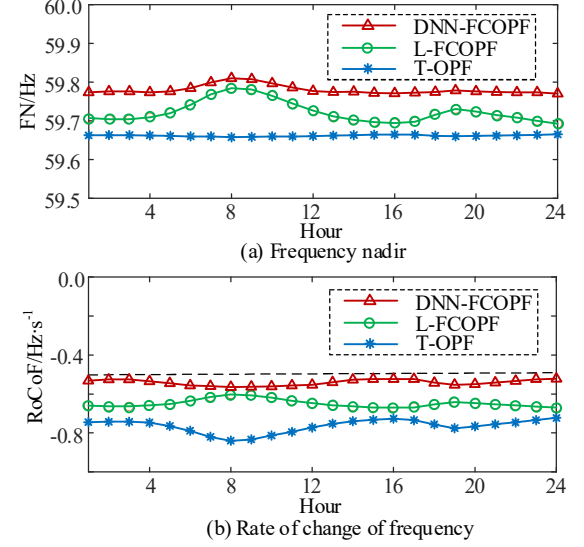


Fig. 10. Comparison of 24-hour (a) frequency nadir, and (b) rate of change of frequency obtained from EMT simulations for the IEEE 39-bus system under T-OPF, L-FCOPF, and DNN-FCOPF frameworks.

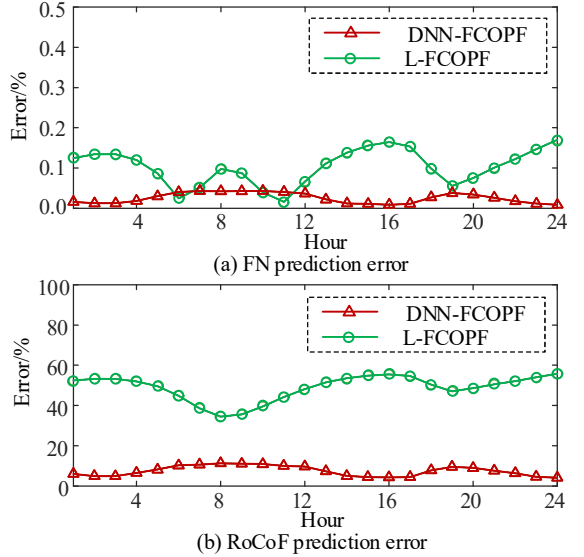


Fig. 11. Relative errors of (a) FN, (b) RoCoF between EMT simulation results and predicted dispatch results under L-FCOPF and DNN-FCOPF.

V. CONCLUSIONS

This paper presents DNN-FP, a deep neural network designed to capture the detailed frequency dynamics of power systems with multiple governors. By integrating this predictor into real-time generation redispatch, the proposed DNN-FCOPF framework significantly enhanced frequency dynamic response compared to the conventional T-OPF with steady-state constraints only, and the L-FCOPF model which relies on simplified analytical calculations. The methodology involves developing a DNN-FP trained on high-fidelity data generated from EMT simulations in PSCAD/EMTDC, followed by its reformulation and integration into a mixed-integer optimization framework. Case studies conducted on the IEEE 9-bus and 39-bus systems demonstrate that the DNN-FCOPF achieves superior accuracy in capturing frequency transients, thereby mark-

edly improving grid stability over the T-OPF and L-FCOPF benchmarks. Building upon these findings, future research will extend the DNN-FCOPF model to inverter-based resources, incorporating grid-following and grid-forming control strategies to address the challenges of low-inertia renewable energy integration.

ACKNOWLEDGMENT

This research was (in part) supported by the National Science Foundation (NSF) under Grant No. 2337598; and it was partly supported by the NSF AI Institute for Advances in Optimization (Award 2112533) and the Georgia Tech Strategic Energy Institute. This work was also in part supported by University of Houston Chevron Energy Graduate Fellows Awards. Any opinions, findings, and conclusions or recommendations expressed in this paper are those of the author(s) and do not necessarily reflect the views of the NSF.

REFERENCES

- [1] F. Jiang, X. Li and P. Van Hentenryck, "A Deep Neural Network-based Frequency Predictor for Frequency-Constrained Optimal Power Flow," *2025 IEEE IAS Annual Meeting*, Taipei, pp. 1-5.
- [2] F. Milano, F. Dörfler, G. Hug, D. J. Hill, and G. Verbić, "Foundations and challenges of low-inertia systems (Invited paper)," *2018 Power Systems Computation Conference (PSCC)*, Jun. 2018, pp. 1-25.
- [3] F. Jiang and X. Li, "Frequency-Dynamics-Aware Economic Dispatch with Optimal Grid-Forming Inverter Allocation and Reserved Power Headroom", Dec. 2025, arXiv:2512.01814 2025. Available: <https://arxiv.org/abs/2512.01814>
- [4] G. Zhang and J. McCalley, "Optimal power flow with primary and secondary frequency constraint," *2014 North American Power Symposium (NAPS)*, Sep. 2014, pp. 1-6.
- [5] Q. Shi, F. Li, and H. Cui, "Analytical Method to Aggregate Multi-Machine SFR Model With Applications in Power System Dynamic Studies," *IEEE Transactions on Power Systems*, vol. 33, no. 6, pp. 6355-6367, Nov. 2018.
- [6] H. Ahmadi and H. Ghasemi, "Security-Constrained Unit Commitment With Linearized System Frequency Limit Constraints," *IEEE Transactions on Power Systems*, vol. 29, no. 4, pp. 1536-1545, Jul. 2014.
- [7] K. Li et al., "Frequency security constrained robust unit commitment for sufficient deployment of diversified frequency support resources," *IEEE Transactions on Industry Applications*, vol. 60, no. 1, pp. 1725-1737, Jan. 2024.
- [8] M. Tuo and X. Li, "Security-constrained unit commitment considering locational frequency stability in low-inertia power grids," *IEEE Transactions on Power Systems*, vol. 38, no. 5, pp. 4134-4147, Sep. 2023.
- [9] G. Cui, Z. Chu, and F. Teng, "Control-mode as a grid service in software-defined power grids: GFL vs GFM," *IEEE Transactions on Power Systems*, vol. 40, no. 1, pp. 314-326, Jan. 2025.
- [10] H. Chávez, R. Baldick, and S. Sharma, "Governor Rate-Constrained OPF for Primary Frequency Control Adequacy," *IEEE Transactions on Power Systems*, vol. 29, no. 3, pp. 1473-1480, May 2014.
- [11] P. M. Anderson and M. Mirheydar, "A low-order system frequency response model," *IEEE Transactions on Power Systems*, vol. 5, no. 3, pp. 720-729, Aug. 1990.
- [12] N. Nguyen, S. Almasabi, A. Bera, and J. Mitra, "Optimal Power Flow Incorporating Frequency Security Constraint," *IEEE Transactions on Industry Applications*, vol. 55, no. 6, pp. 6508-6516, Nov. 2019.
- [13] Z. Zhang, M. Zhou, Z. Wu, S. Liu, Z. Guo, and G. Li, "A frequency security constrained scheduling approach considering wind farm providing frequency support and reserve," *IEEE Transactions on Sustainable Energy*, vol. 13, no. 2, pp. 1086-1100, Apr. 2022.
- [14] L. Sang, Y. Xu, Z. Yi, L. Yang, H. Long, and H. Sun, "Conservative Sparse Neural Network Embedded Frequency-Constrained Unit Commitment With Distributed Energy Resources," *IEEE Transactions on Sustainable Energy*, vol. 14, no. 4, pp. 2351-2363, Oct. 2023.
- [15] X. Zhao, H. Wei, J. Qi, P. Li, and X. Bai, "Frequency Stability Constrained Optimal Power Flow Incorporating Differential Algebraic Equations of Governor Dynamics," *IEEE Transactions on Power Systems*, vol. 36, no. 3, pp. 1666-1676, May 2021.
- [16] B. Zhou, R. Jiang, and S. Shen, "Frequency Stability-Constrained Unit Commitment: Tight Approximation Using Bernstein Polynomials," *IEEE Transactions on Power Systems*, vol. 39, no. 4, pp. 5907-5919, Jul. 2024.
- [17] L. Fang, F. Jiang, A. Toms, and X. Li, "Analysis of Learning-based Offshore Wind Power Prediction Models with Various Feature Combinations", *IEEE PES General Meeting*, Austin, TX, USA, Jul. 2025.
- [18] C. Li et al., "Optimal Power Flow in a highly renewable power system based on attention neural networks," *Applied Energy*, vol. 359, p. 122779, Apr. 2024.
- [19] J. Rahman, C. Feng, and J. Zhang, "Machine Learning-Aided Security Constrained Optimal Power Flow," *2020 IEEE Power & Energy Society General Meeting (PESGM)*, Aug. 2020, pp. 1-5.
- [20] T. Pham and X. Li, "Reduced Optimal Power Flow Using Graph Neural Network," *2022 North American Power Symposium (NAPS)*, Oct. 2022, pp. 1-6.
- [21] M. Tuo and X. Li, "Deep Learning based Security-Constrained Unit Commitment Considering Locational Frequency Stability in Low-Inertia Power Systems", *54th North American Power Symposium*, Salt Lake City, UT, USA, Oct. 2022.
- [22] Y. Zhang et al., "Encoding Frequency Constraints in Preventive Unit Commitment Using Deep Learning With Region-of-Interest Active Sampling," *IEEE Transactions on Power Systems*, vol. 37, no. 3, pp. 1942-1955, May 2022.
- [23] B. She, F. Li, H. Cui, J. Wang, Q. Zhang, and R. Bo, "Virtual Inertia Scheduling (VIS) for Real-Time Economic Dispatch of IBR-Penetrated Power Systems," *IEEE Transactions on Sustainable Energy*, vol. 15, no. 2, pp. 938-951, Apr. 2024.
- [24] T. Amraee, M. G. Darebaghi, A. Soroudi, and A. Keane, "Probabilistic under frequency load shedding considering RoCoF relays of distributed generators," *IEEE Trans. Power Syst.*, vol. 33, no. 4, pp. 3587-3598, Jul. 2018.
- [25] F. Milano, "Rotor speed-free estimation of the frequency of the center of inertia," *IEEE Transactions on Power Systems*, vol. 33, no. 1, pp. 1153-1155, Jan. 2018.
- [26] Q. Shi, F. Li, and H. Cui, "Analytical Method to Aggregate Multi-Machine SFR Model with Applications in Power System Dynamic Studies," *IEEE Transactions on Power Systems*, vol. 33, no. 6, pp. 6355-6367, Nov. 2018.
- [27] Z. Zhang, M. Zhou, Z. Wu, S. Liu, Z. Guo, and G. Li, "A frequency security constrained scheduling approach considering wind farm providing frequency support and reserve," *IEEE Transactions on Sustainable Energy*, vol. 13, no. 2, pp. 1086-1100, Apr. 2022.
- [28] C. Zhao, F. Jiang and X. Li, "Linearization of ReLU Activation Function for Neural Network-Embedded Optimization: Optimal Day-Ahead Energy Scheduling", arXiv:2310.01758, Oct. 2023
- [29] Manitoba Hydro International Ltd., "IEEE 09 Bus System", May 22, 2018. [Online]. Available: <https://www.pscad.com/knowledge-base/article/25>
- [30] PowerWorld Corporation, "Powerworld simulator 18 block diagrams," 2014. [Online]. Available: <http://www.powerworld.com/files/BlockDiagrams-18.pdf>
- [31] "IEEE Recommended Practice for Excitation System Models for Power System Stability Studies," in IEEE Std 421.5-2016 (Revision of IEEE Std 421.5-2005), vol., no., pp.1-207, 26 Aug. 2016.
- [32] J. Lu and X. Li, "Transmission Expansion Planning for Renewable-Energy-Dominated Power Grids Considering Climate Impact", *Journal of Modern Power Systems and Clean Energy*, vol. 12, no. 6, pp. 1737-1748, Nov. 2024.
- [33] Anantha Pai. Energy Function Analysis for Power System Stability. Springer, 1989.